



Three-dimensional density tomography determined from multi-directional muography of the Omuroyama scoria cone, Higashi-Izu monogenetic volcano field, Japan

Shogo Nagahara^{1,2} · Seigo Miyamoto² · Kunihiro Morishima³ · Toshiyuki Nakano³ · Masato Koyama⁴ · Yusuke Suzuki⁵

Received: 22 May 2022 / Accepted: 15 August 2022 / Published online: 20 September 2022
© The Author(s) 2022

Abstract

Scoria cone is one of the basic forms of volcanoes, and clarifying its detailed internal structure and magma movement during its formation is important for understanding the nature of eruptions and also for volcanic disaster mitigation. We conducted a multi-directional muographic survey of the Omuroyama scoria cone, Japan, in order to determine the three-dimensional density structure of the scoria cone. We used a nuclear emulsion detector optimized for multi-directional muography that was installed at 11 sites around the volcano. Muon tracks recorded on emulsion films were read with a high-speed automated readout system. We obtained the three-dimensional density structure by applying a linear inversion to the muographic images, and evaluated the uncertainties. High-density zones were detected in scoria cone. Based on these observations and detailed topographic and geological constraints, we infer that high-density zones are the central, highly welded vent of the scoria cone, three-directional radial dikes extending from the central vent, respectively. We also infer that an E-W-trending dike fed a small lava flow, and that a SSE-NNW-trending dike caused a small flank eruption and produced a crater on the flank of the cone. Our results visualize the three-dimensional internal structure of volcanoes with novel resolution, and thereby demonstrate that the formation process of volcanoes can be discussed in detail. Since it has been difficult to directly detect such clear visualization of the internal structures and eruptive processes in the past, multi-directional muography has resulted in providing one hope for understanding volcanic activity.

Keywords Emulsion · Cosmic ray · Inversion · Internal structure · Eruptive process

要旨

スコリア丘は火山の基本形の一つであり、その詳細な内部構造や形成時のマグマの動きを明らかにすることは、噴火の本質を理解する上で、また火山災害の軽減のためにも重要である。我々は大室山スコリア丘の3次元密度構造を明らかにするため、多方向ミュオグラフィ観測を行った。観測では多方向ミュオグラフィに最適化された原子核乾板検出器を11か所設置した。原子核乾板に記録されたミュオン飛跡は高速自動読み取り装置で読み出した。得られたミュオグラフィ画像に線形インバージョンを用いて3次元密度構造を求め、その不定性を評価した。その結果、スコリア丘内部に高密度領域が検出された。この観測結果と詳細な地形・地質学的な制約から、高密度領域は溶結度の高い中心火道と、そこから3方向に伸びる放射状岩脈であると推定した。また、西に伸びる岩脈が山体西麓の小溶岩流を形成し、南南東に伸びる岩脈が小さな側噴火を起こして南山腹の小火口

Editorial responsibility: V. Acocella

✉ Shogo Nagahara
nagahara@radix.h.kobe-u.ac.jp

¹ Graduate School of Human Development and Environment,
Kobe University, Kobe, Japan

² Earthquake Research Institute, The University of Tokyo,
Tokyo, Japan

³ Fundamental Particle Physics Laboratory, Graduate School
of Science of Nagoya University, Nagoya, Japan

⁴ Center for Integrated Research and Education of Natural
Hazards, Shizuoka University, Shizuoka, Japan

⁵ STORY, Ltd., Tokyo, Japan

を形成したと推定した。本研究の成果は、火山の3次元内部構造をこれまでにない解像度で可視化することで、火山の形成過程を詳細に議論できることを示すものである。従来、このような内部構造や噴火過程を明確に可視化することは直接的には困難であったが、多方向ミュオグラフィは火山活動の理解に一つの道筋を与えた。

キーワード 原子核乾板・宇宙線・インバージョン・内部構造・噴火プロセス

Introduction

Scoria cones are a type of monogenetic volcano that occurs worldwide. Previous studies of scoria cones have revealed a variety of internal structures and developmental processes, and the factors responsible for these features are partly understood (McGetchin et al. 1974; Yamamoto 2003; Kereszturi and Nemeth 2013; Smith and Nemeth 2017). However, these studies are mostly based on fragmented outcrops and remnants of cones, where much of the edifice has already been eroded. There have been few case studies of cross-sections of scoria cones from multiple directions that can examine the relationships with the dikes and lava flows associated with the scoria cone. One of the most significant examples is a study that clarified the three-dimensional relationships between the central conduit of the Puy de Lemptegy scoria cone and the dikes and lava flows derived from it, including the direction of magma movement, were determined from a well-exposed and well-preserved quarry site (Petronis et al. 2013; Delcamp et al. 2014). However, this is a rare case due to the small size of the scoria cone and the fortunate fact that the entire quarry site was preserved without planting. The detailed, three-dimensional, inner structures of large scoria cones (i.e., edifices with talus slopes classified as developmental stages 3–4 in McGetchin et al. (1974)) have not been determined.

A few studies have conducted indirect geophysical exploration of interior of scoria cones. Hashimoto et al. (2009) obtained the resistivity and magnetic structures of Komezuka scoria cone on Aso Volcano by electromagnetic surveys. This study identified a high-density area in the center of the scoria cone, which was presumed to be welded, and showed that the central conduit was not connected to the surrounding lava flow, at least in the shallow part of the cone. Barde-Cabusson et al. (2013) conducted an electrical survey of three scoria cones in Spain and obtained results that identified a central conduit and surrounding welded rocks. Bolós et al. (2020) summarized the results of a self-potential, ground-temperature, and a 3D resistivity model geophysical survey on the Parícutin scoria cone, and they understood the surface structure and detected zones of convective hydrothermal fluid circulation in the subsurface. However, in these cases, the inner structure of the cones was only roughly estimated by comparison with the structures observed in geological surveys of other volcanoes.

Muography has rapidly developed since the twenty-first century as an exploration method that can reveal the internal structures of large objects (Tanaka et al. 2007a). This technique uses the absorption of cosmic ray muons in matter to measure the density distribution like an X-ray image. The attenuation of the muon flux depends on the amount of material along the path of the muon (i.e., the density length). The energy spectrum of the incident cosmic ray muon (Honda et al. 2004) and its interaction with matter (Groom et al. 2001) allows the density length to be obtained from measurements of the penetrating muon flux.

Unidirectional muography has been conducted at numerous volcanoes (Mt. Asama; Tanaka et al. 2007b; Showa-Shinzan lava dome; Tanaka et al. 2007c; Satsuma–Iwojima; Tanaka et al. 2009, 2014; Sakurajima; Oláh et al. 2018; Puy de Dôme; Carloganu et al. 2013; Ambrosino et al. 2015; Stromboli; Tioukov et al. 2019). These observations only obtained two-dimensional projection images like radiographs. To solve this problem, Tanaka et al. (2010) undertook muography from two directions. Other studies also used a combination of muography and gravity observations, which are also sensitive to the density (Nishiyama et al. 2014a, 2017; Rosas-Carbajal et al. 2017). However, these approaches were poor three-dimensional resolution. For example, the resolution of Rosas-Carbajal et al. 2017 is approximately 500 m. The simulation of Nagahara and Miyamoto (2018) showed that in order to solve this problem and obtain an appropriate three-dimensional density distribution, it is necessary to conduct muographic observations in multiple directions, as the case for X-ray computed tomography. For example, they showed that observing from 64 directions would provide a spatial resolution of 10 to 20 meters.

Such multi-directional observations are difficult due to detector limitations, but have become feasible in recent years with the rapid development of muon detectors. In order to perform multi-directional muographic observations of volcanoes, it is necessary to install the detectors in places where infrastructure is not available. Nuclear emulsion muon detectors are compact, lightweight, and do not require a power supply, which makes these suitable for multi-directional observations. With the development of related technologies in recent years (Hamada et al. 2012; Yoshimoto et al. 2017), emulsion detectors have also become increasingly larger in scale (for example, Khufu's Pyramid; Morishima et al. 2017).

Scoria cones are suitable targets for multi-directional muography. Given that the interiors of scoria cones are

expected to have a complex structure due to diking and welding (Kereszturi and Németh 2016). It is challenging to explore their structures with conventional muographic observations. However, multi-directional muography might allow scoria cones with complex structures to be robustly investigated.

We selected the Omuroyama scoria cone ($34^{\circ} 54' 11''$ N, $139^{\circ} 05' 40''$ E; 580 m above sea level.), which is the largest monogenetic scoria cone in the Higashi-Izu monogenetic volcano field located in Shizuoka Prefecture, Japan (Koyama and Umino 1991), for a multi-directional muographic study (Fig. 1). The diameter of the foot of the edifice is about 1 km, and the height from the bottom is 300 m. There is a summit crater with a diameter of ca. 300 m and a depth of ca. 50 m. The summit crater is surrounded by straight slopes that strongly suggest its talus origin. Saito et al. (2003) estimated the eruption age of the cone to be ~ 4 ka, based on radiocarbon dating.

The eruptive history of the Omuroyama scoria cone has generally been constrained by the previous field geological survey (Koyano et al. 1996). The process of the eruption of the volcano can be divided into five stages (A to E), based on tephra stratigraphy. In addition, associated lava flows were divided into lava flows I to IV. The eruptive history is as follows.

Eruption of the Omuroyama scoria cone began with a subplinian eruption (stage A) and a short period of deposition of volcanic ash (stage B). Strombolian eruptions then continued for a protracted period, which formed a large scoria cone and lava flows I–III from three locations at the foot of the cone (stages C–D). Lava flows II and III formed the Izu Kogen lava plateau and Jogasaki lava coast, respectively, and finally the Iwamuroyama and Moriyama plug domes formed on the source craters of lava flows II and III, respectively. At the end of stage D, a lava lake was formed in the summit crater, which then drained. Part of the drained lava leaked into the western foot of the cone, which produced a small-scale lava flow (lava flow IV). Finally, the volcanic activity ended with a small explosion on the southern flank of the cone, which formed a small crater (stage E).

Because no strata showing significant dormant periods of eruptive activity have been identified in the tephra succession of the Omuroyama scoria cone, Koyano et al. (1996) also concluded that the Omuroyama scoria cone should be a monogenetic volcano and its eruption time was estimated to be a few years, 20 to 30 years at the most.

Although the Omuroyama scoria cone has an apparently well-proportioned cone-shaped edifice, a small ridge

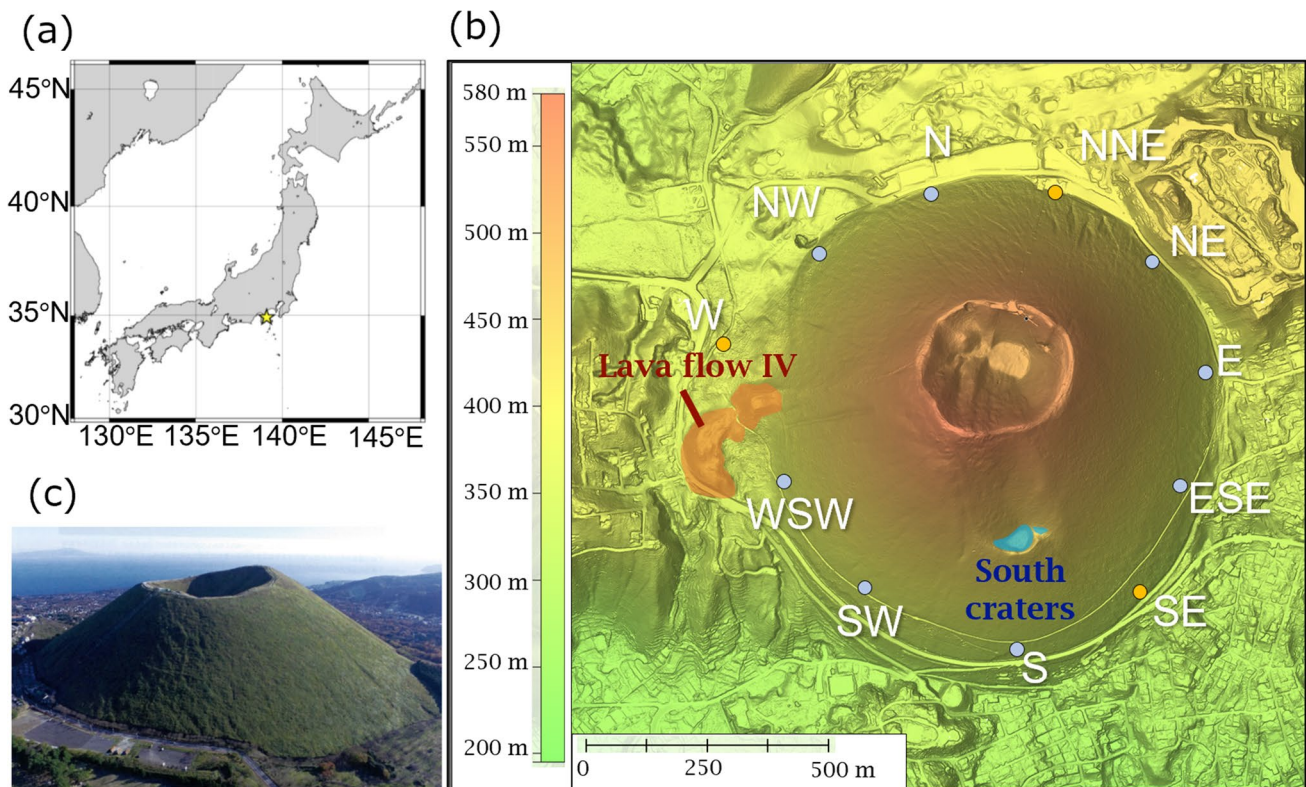


Fig. 1 **a** The location of the Higashi-Izu monogenetic volcano field (star symbol) in Japan. The summit of the scoria cone is $34^{\circ} 54' 11''$ N, $139^{\circ} 05' 40''$ E. **b** Elevation map of the Omuroyama scoria cone. The yellow and blue dots are the observation points in 2018 and

2019, respectively. The orange and blue areas show the lava flow IV and south craters, respectively. **c** The picture of Omuroyama from northwestern side (photo's by Koyama)

on its western foot, a small crater on the southern flank, and the complex topography of the summit crater imply a complex formation history and inner structures (Fig. 1). In typical basaltic rocks, the density of the non-welded scoria deposits is expected to be $0.5\text{--}1.0 \times 10^3 \text{ kg/m}^3$, whereas the density of the lava flows and welded scoria are expected to be $>2.0 \times 10^3 \text{ kg/m}^3$. With this amount of density contrast, we can expect to obtain a resolution of less than 100 m by muography from a dozen or more directions (Nagahara and Miyamoto, 2018). In addition, no mountains, which would interfere with the muographic observations, exist behind the Omuroyama scoria cone in any direction within a radius of 4 km. Therefore, the Omuroyama scoria cone is an ideal target for multi-directional muography.

We undertook multi-directional muographic observations of the Omuroyama scoria cone and used the data to obtain a three-dimensional density reconstruction using linear inversion techniques. In addition, we used our reconstruction, the latest topographic data, and field geological surveys to constrain the eruption history of the Omuroyama scoria cone since its formation.

Methods

Overview of multi-directional muography

The multi-directional muography and analysis of the results can be divided into several steps. Figure 2 shows the steps taken when using emulsion detector and related previous

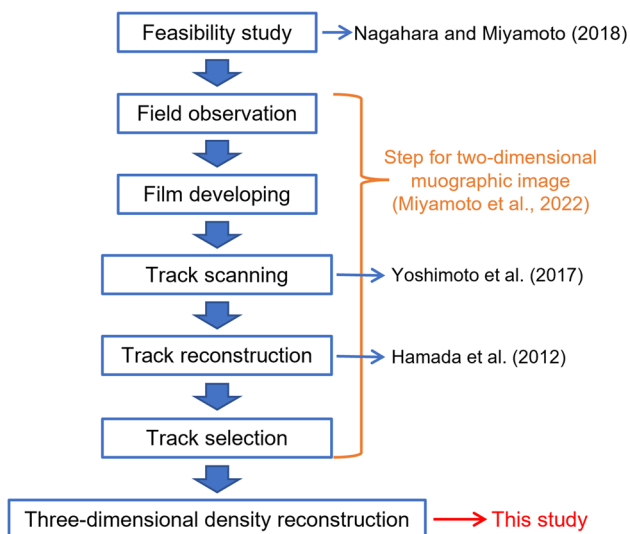


Fig. 2 Procedure for performing multi-directional muography. The feasibility study is shown in detail in Nagahara and Miyamoto (2018). The obtaining of two-dimensional muographic images is shown in detail in Miyamoto et al. (2022), track scanning is shown in Yoshimoto et al. (2017), and track reconstruction is shown in Hamada et al. (2012), respectively

studies. A feasibility study on Omuroyama is described in Nagahara and Miyamoto (2018). The procedure to obtain the two-dimensional muographic images is described in Miyamoto et al. (2022). Three-dimensional density reconstruction and its interpretation is described in a later section of this paper.

Muographic observations

The muographic observations were performed in 2018 and 2019. The detail of muon detector, the installation of detectors, and analysis are described in Miyamoto et al. (2022). Figure 1 shows the installed stations. To calculate the path length, we used a 1-m resolution digital elevation model (DEM) using an airborne LiDAR survey obtained in 2009 by the Numazu Office of River and National Highway, Ministry of Land, Infrastructure, Transport and Tourism.

The detector was newly constructed based on the structure of an emulsion cloud chamber (ECC; Nishiyama et al. 2014b). Because the background noise that affects muographic studies is due to protons, electrons, and muons with energies of $<1 \text{ GeV}$ (Nishiyama et al. 2016; Niess, 2022), 1-mm-thick lead plates were stacked between the nuclear emulsions. In this study, 20 emulsions with sizes of $10 \text{ cm} \times 12.5 \text{ cm}$ and 19 lead plates of the same size were alternately stacked (Miyamoto et al. 2022).

After the observations, the nuclear emulsion films were developed and the recorded tracks were read using the hyper-track selector (HTS; Yoshimoto et al. 2017). Reconstruction of the tracks was performed with NETSCAN 2.0 software (Hamada et al. 2012). We then selected the muon tracks and estimated the muon detection efficiency (Miyamoto et al. 2022).

The ratio of the observed/expected muon counts in the free sky region was calculated for each 100-mrad angular bin, and the mean value was used as the calibration value and the deviation as the calibration error (Table 1). Only ECC_C (station NNE) had a larger calibration error than the other detectors. We subsequently analyzed the data from 10 of the 11 sites, excluding this station.

We calculated the density length using the following procedure.

1. We calculated a numerical table of the relationship between the mean density and muon counts for each angular bin using the energy spectrum of the incident cosmic ray muons from Honda et al. (2004), their interaction with matter from Groom et al. (2001), and topographic data for the Omuroyama scoria cone.
2. We multiplied the expected muon counts by the calibration value of the ECC.
3. We determined the density length that matched the observed muon counts.

Table 1 calibration values and errors for each emulsion cloud chamber

| ECC | Site | Calibration value | Calibration error |
|--------|------|-------------------|-------------------|
| ECC_A | SE | 0.83 | 0.19 |
| ECC_B | W | 0.88 | 0.08 |
| ECC_C | NNE | 0.67 | 0.33 |
| ECC_01 | N | 0.89 | 0.09 |
| ECC_02 | N | 0.93 | 0.08 |
| ECC_03 | NW | 0.90 | 0.06 |
| ECC_04 | NW | 0.88 | 0.05 |
| ECC_05 | WSW | 0.84 | 0.10 |
| ECC_06 | WSW | 0.79 | 0.09 |
| ECC_07 | SW | 0.81 | 0.08 |
| ECC_08 | SW | 0.80 | 0.07 |
| ECC_09 | S | 0.79 | 0.08 |
| ECC_10 | S | 0.87 | 0.07 |
| ECC_11 | ESE | 0.90 | 0.07 |
| ECC_12 | ESE | 0.90 | 0.07 |
| ECC_13 | E | 0.97 | 0.06 |
| ECC_14 | E | 0.96 | 0.07 |
| ECC_15 | NE | 0.92 | 0.06 |
| ECC_16 | NE | 0.94 | 0.06 |

An example of the two-dimensional muographic results is shown in Fig. 3. The overall density of the Omuroyama scoria cone was $1.39 \pm 0.01 \times 10^3 \text{ kg/m}^3$. This is in good agreement with the value obtained by Nishiyama et al. (2020) ($1.39 \pm 0.07 \times 10^3 \text{ kg/m}^3$) from gravity observations.

Inversion method

The three-dimensional density reconstruction was undertaken using the observed muon counts based on the methodology presented in this section.

Three-dimensional density inversion method

We used the linear inversion method of Nishiyama et al. (2014a). The density length d can be written as follows:

$$d = \int_{\tau} \rho(\xi) d\xi, \tag{1}$$

where ρ is the density, τ is the muon path, and ξ is the coordinate along the trajectory τ . The region of reconstruction is subdivided into J voxels of density ρ_j ($j = 1, 2, \dots, J$). The density length of path i ($i = 1, 2, \dots, I$) can be written as follows:

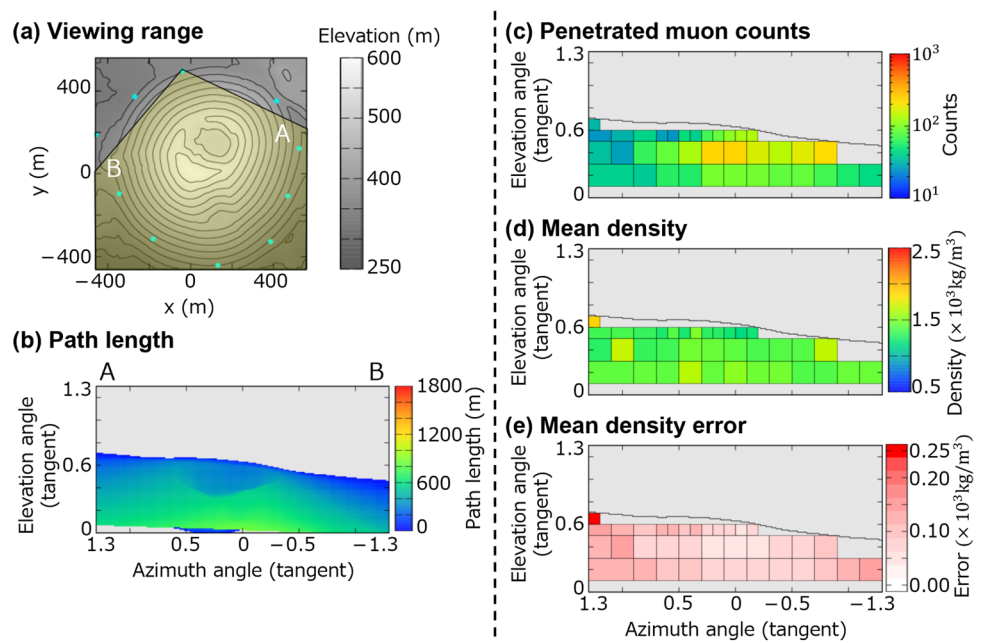
$$d_i = \sum_{j=1}^J A_{ij} \rho_j, \tag{2}$$

where d_i is density length of path i and A_{ij} is the length of the i th path across the j th voxel. Equation 2 can also be written as follows:

$$\mathbf{d} = \mathbf{A}\rho, \tag{3}$$

where \mathbf{d} is the data vector, \mathbf{A} is the observation matrix, and ρ is the voxel density. Nishiyama et al. (2014a) used a Bayesian approach to solve this inverse problem (Tarantola and

Fig. 3 Two-dimensional muographic results at station N. **a** Map of the topography and viewing range. **b** Path length of the scoria cone. **c** The muon counts. The black line represents the shape of the scoria cone. The bin size was adjusted such that the muon count was at least 25. The measurement area was set at an elevation angle of 100mrad (5.7°) or greater. **d** The obtained density distribution. **e** The density error caused by the number of observed muons



Nercessian, 1984). When the observed data d_{Obs} is obtained, the solution of Eq. 3 is as follows:

$$\rho' = \rho_0 + \left({}^t\mathbf{A}\mathbf{C}_d^{-1}\mathbf{A} + \mathbf{C}_\rho^{-1} \right)^{-1} {}^t\mathbf{A}\mathbf{C}_d^{-1} (d_{\text{Obs}} - \mathbf{A}\rho_0), \quad (4)$$

$$\mathbf{C}_{\rho'} = \left({}^t\mathbf{A}\mathbf{C}_d^{-1}\mathbf{A} + \mathbf{C}_\rho^{-1} \right)^{-1}, \quad (5)$$

where ρ_0 is the initially guessed density, \mathbf{C}_d is the data covariance matrix, \mathbf{C}_ρ is a covariance matrix for the initial guess, and $\mathbf{C}_{\rho'}$ is posterior covariance matrix. Nishiyama et al. (2014a) imposed a smoothing constraint through an exponential covariance on $\mathbf{C}_{\rho'}$, based on Tarantola and Nercessian (1984):

$$C_\rho(j_1, j_2) = \sigma_\rho^2 \exp\left(-\frac{D(j_1, j_2)}{l}\right), \quad (6)$$

where σ_ρ is the magnitude of the uncertainty, l is the correlation length, and $D(j_1, j_2)$ is the distance between the j_1 th and j_2 th voxels. Procedures for determining the optional parameters, l and σ_ρ , are described in later sections.

In this method, the muon arrival direction is represented by the center of the angular bin because density length cannot be defined for a finite range of solid angles. This is not a good approximation when the angular resolution of the muographic data is poor. To solve this problem, we defined the observation matrix in terms of the number of observed muons per angular bin. The i th observed muon count is the sum of the muon numbers in the smaller angular bins i_i . Therefore, we first prepared an observation matrix with the observed muon counts for i_i , and then summed over i to calculate the observation matrix for the observed muon counts of the solid angle Ω_i (Fig. 4).

The relationship between the cosmic ray muon flux attenuation and density length is nonlinear (Tanaka et al. 2007b). Therefore, the density distribution within the scoria cone is linearized here for the case of ρ_0 . When the

relationship between the muon number N and density length d is $N_{\text{Obs}} = f(d)$, the density length when the density distribution is ρ_0 is d_0 , the muon count is N_{Obs}^0 , and the observed muon count in the angular bin i_i is as follows:

$$N_{i_i} = N_{i_i}^0 + \delta N_{i_i} \approx f_{i_i}(d_{i_i}^0) + (d_{i_i} - d_{i_i}^0) \frac{\partial f_{i_i}}{\partial d_{i_i}}(d_{i_i}^0). \quad (7)$$

Using this and Eq. 2, the observation matrix for the number of observed muons A^N can be expressed as follows:

$$A_{i_i j}^N = \frac{\partial f_{i_i}}{\partial d_{i_i}}(d_{i_i}^0) A_{i_i j}. \quad (8)$$

Summing this over i , we obtain the observation matrix for the solid angle Ω_i :

$$A_{ij}^N = \sum_{i=1}^{i_M} A_{i_i j}. \quad (9)$$

In this case, the data covariance matrix for the muon counts is as follows:

$$C_N(i_1, i_2) = \begin{cases} \sigma_{N_i}^2 & (i_1 = i_2 = i) \\ 0 & (i_1 \neq i_2) \end{cases}, \quad (10)$$

where $\sigma_{N_i}^2$ is the error of N_i for the i -th solid angle area.

From the above, the formula for the three density reconstruction is:

$$\rho' = \rho_0 + \left({}^t\mathbf{A}\mathbf{C}_N^{-1}\mathbf{A} + \mathbf{C}_\rho^{-1} \right)^{-1} {}^t\mathbf{A}\mathbf{C}_N^{-1} (N_{\text{Obs}} - \mathbf{A}\rho_0), \quad (11)$$

$$\mathbf{C}_{\rho'} = \left({}^t\mathbf{A}\mathbf{C}_N^{-1}\mathbf{A} + \mathbf{C}_\rho^{-1} \right)^{-1}, \quad (12)$$

The calculations for this analysis can be done on a laptop, but multiple calculations are required to determine optional parameters. The method of determining the parameters in this study is described in a later section.

Topographic and geological survey

To interpret the muographic results, we undertook new detailed topographical and geological surveys of the Omuroyama scoria cone and surrounding region. For the topographic analysis, we created a high-resolution DEM (10-cm mesh), based on the point cloud data acquired by Shizuoka Prefecture using an airborne LiDAR survey in 2019 (<https://www.geospatial.jp/ckan/dataset/shizuoka-2019-pointcloud>). A field geological survey was also conducted from January to June 2021 to interpret the geomorphic features. Their results are shown in the later section.

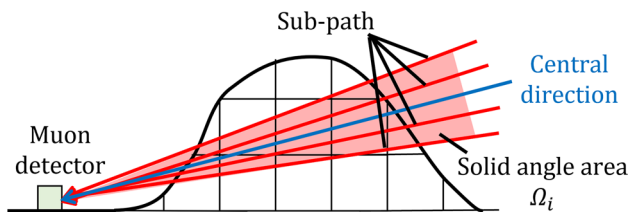


Fig. 4 Schematic view of the solid angle area. Red area is the solid angle area. Blue line is the central direction in solid angle area. Red lines are sub paths in solid angle area

Results

Three-dimensional density reconstruction

The inversion method was applied to the muographic results from 10 directions and 3D density reconstruction was performed. In this subsection, we describe the determination of the reconstruction parameters (l and σ_ρ) using the observed data, the resulting estimation of uncertainties, and the results of the resolution estimation.

Parameter determination

For the three-dimensional density reconstruction, we selected the following parameters: voxel size of $20 \times 20 \times 20$ m, $\rho_0 = 1.39 \times 10^3 \text{ kg/m}^3$, $\sigma_\rho = 0.3 \times 10^3 \text{ kg/m}^3$, and $l = 70$ m. For ρ_0 , we used the observed value of the overall density. The above values were selected by searching for parameters for l in increments of 10 m from 10 to 200 m, and for σ_ρ in increments of $0.1 \times 10^3 \text{ kg/m}^3$ from 0.1

to $1.0 \times 10^3 \text{ kg/m}^3$. The three-dimensional density reconstruction results for each parameter are shown in Fig. 5.

The correlation length was determined by requiring that the amount of information in the three-dimensional density reconstruction results and observed data be equal. Therefore, the amount of information in the three-dimensional density reconstruction results was considered to be the number of voxels when the length of one side of the voxel was the correlation length. Given that the correlation length at which the amount of information in the three-dimensional density reconstruction is equal that in the observed data is 63.6 m, we selected 70 m.

We constrained the value of σ_ρ in two ways. The first constraint is that the results of the three-dimensional density reconstruction should have realistic values. In this case, the constraint was that $> 90\%$ of the voxels should have densities of $0.5\text{--}3.0 \times 10^3 \text{ kg/m}^3$. As a result, $\sigma_\rho = 0.1\text{--}0.4 \times 10^3 \text{ kg/m}^3$ was applicable at $l = 70$ m. The second constraint is that the structure is reconstructed by simulations assuming a 100-m diameter, $2.5 \times 10^3 \text{ kg/m}^3$ density cylinder structure on a mountain body of $1.3 \times 10^3 \text{ kg/m}^3$ density. The simulation results for the 450-m-elevation section are shown in

Fig. 5 Reconstructed images in the case where $\rho_0 = 1.39 \times 10^3 \text{ kg/m}^3$, $l = 70\text{--}100$ m, and $\sigma_\rho = 0.1\text{--}0.5 \times 10^3 \text{ kg/m}^3$, which is at an elevation of 450 m. The blue dots represent the locations of the observation points, and the black lines represent the contours of the scoria cone in the cross-section

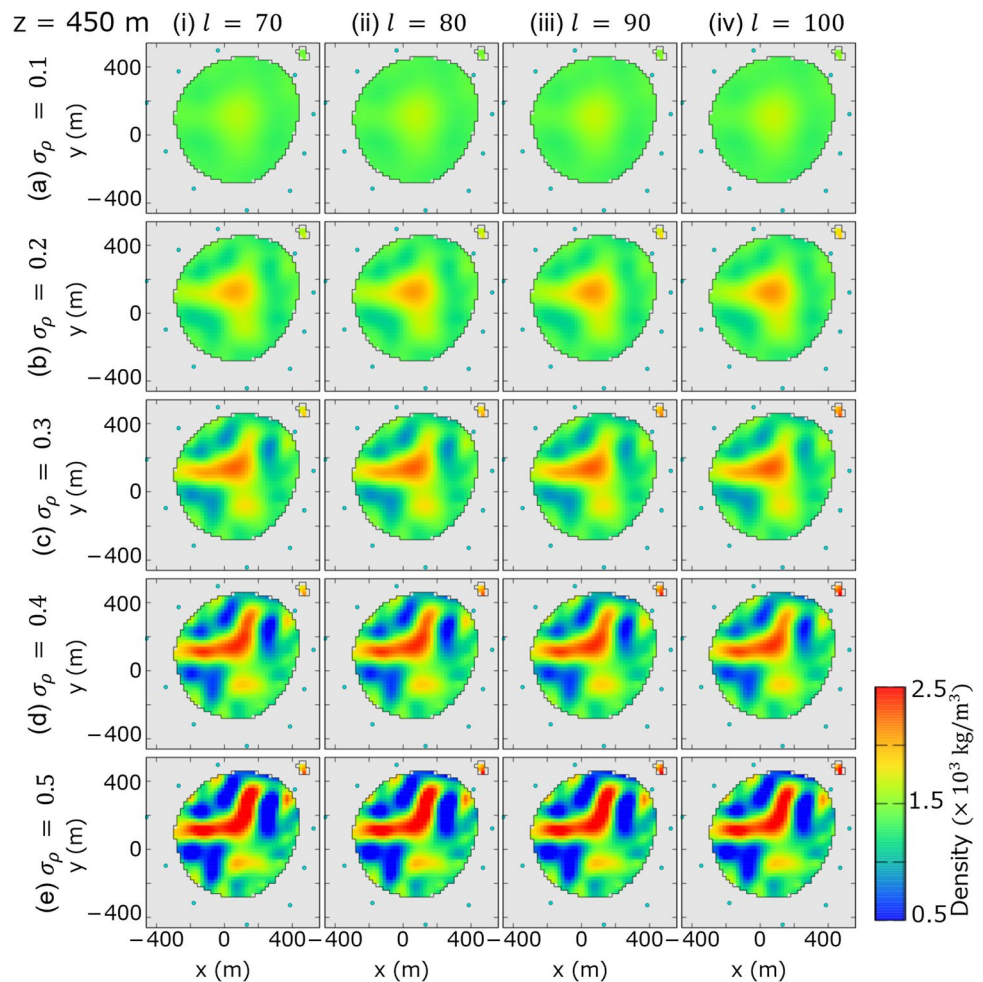


Fig. 6 A simulation in the case where $l = 70\text{--}100$ m and $\sigma_\rho = 0.1\text{--}0.5 \times 10^3$ kg/m³, which is at an elevation of 450 m. The structure was assumed to be cylindrical with a diameter of 100 m and density of 2.5×10^3 kg/m³ below $z = 500$ m, with a density of 1.3×10^3 kg/m³. The blue dots represent the locations of the observation points, and the black lines represent the contours of the scoria cone in the cross-section

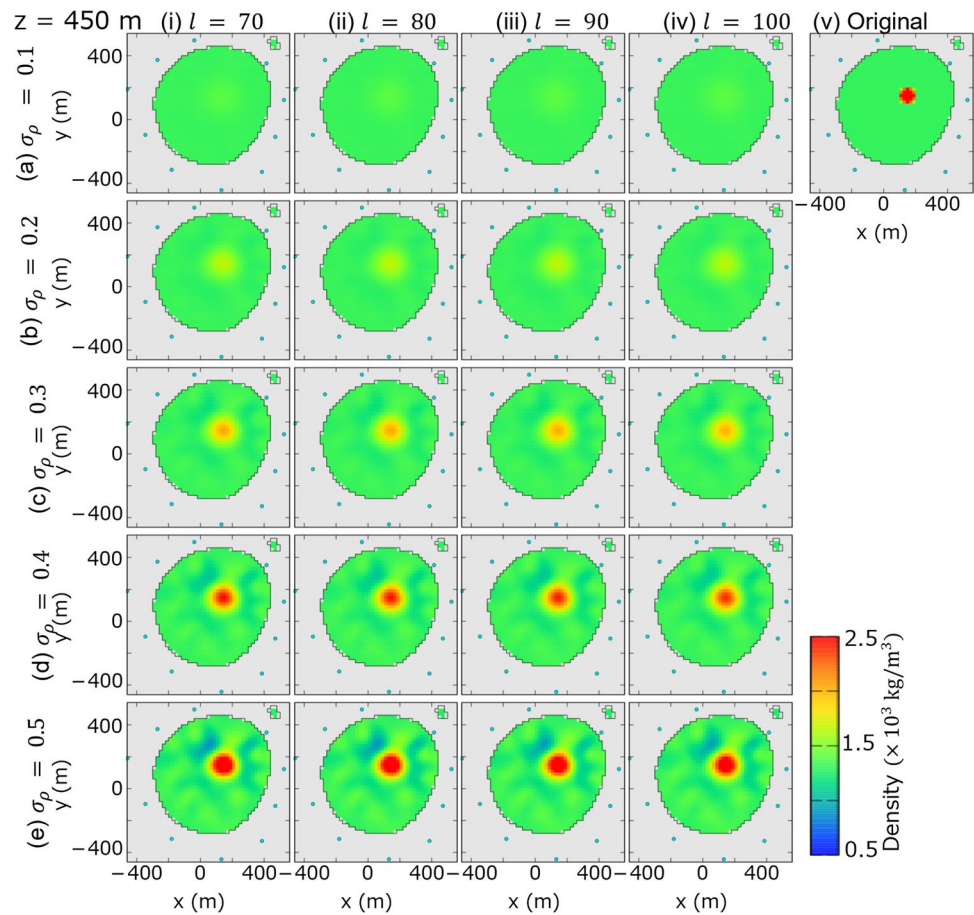


Fig. 6. As a result, the cylindrical structure was not reconstructed for $\sigma_\rho = 0.1 \times 10^3$ kg/m³. From these considerations, we conclude that $\sigma_\rho = 0.2\text{--}0.4 \times 10^3$ kg/m³. In this range, the density contrast changed, but there was no significant difference in the density structure. Therefore, we selected the central value of 0.3×10^3 kg/m³.

Uncertainties

The three-dimensional density reconstruction results include a variety of uncertainties. In this paper, the following three uncertainties were considered.

The first uncertainty is the covariance matrix. The propagation of the accidental error on the observed data is represented by the diagonal component of the covariance matrix, which is represented by Eq. 11. The resulting uncertainty was $0.2\text{--}0.3 \times 10^3$ kg/m³ throughout the scoria cone.

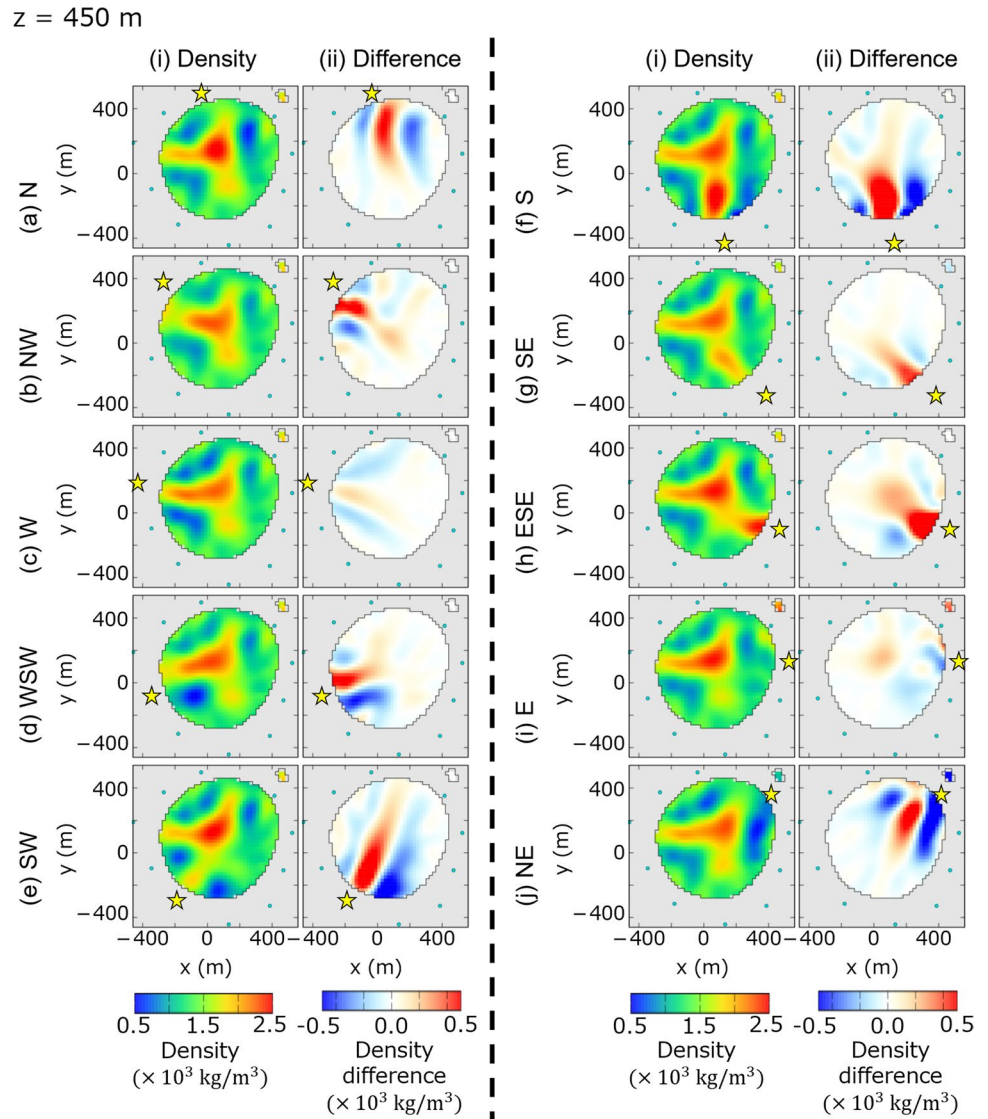
The second uncertainty is ρ_0 . In this study, we used ρ_0 as the observed value of the overall density. There is an uncertainty on ρ_0 that can be assigned. In this case, the variation of the overall density determined for each observation point was taken into account. The difference between the results of the three-dimensional density reconstruction for $\rho_0 = 1.35$ and 1.44×10^3 kg/m³, and those for $\rho_0 = 1.39 \times 10^3$ kg/m³

was adopted as the second uncertainty. The uncertainty was less than 0.1×10^3 kg/m³ and smaller than that of the covariance matrix.

The third uncertainty is the stability of the solution depending on location of the observation points. In a three-dimensional density reconstruction obtained by an inversion method, some artificial noise can characterize locations with little observational information. In order to evaluate the effect of artificial noise related to the station configuration, we performed three-dimensional density reconstructions using 9 observation points by removing 1 of the 10 observation points, and examined the changes in the density reconstructions. The results are shown in Fig. 7. It was found that high-density regions tend to form in front of the removed observation point and low-density regions form on both sides of the observation point. In this study, the uncertainty of each voxel was defined by the value of the largest density change of these 10 analysis results.

The three uncertainties were assumed to be independent. The square root of the sum of the squares of the above three uncertainties was taken as the overall uncertainty of the three-dimensional density reconstructions, and the results and topography from the 10 cm DEM are shown in Fig. 8. The high-density structures identified by the muography

Fig. 7 (i) Reconstructed images and (ii) the density difference when 1 of the 10 detectors is removed. The blue dots indicate the locations of the observation points used in the analysis, and the stars indicate the locations of the excluded observation points. The black lines represent the contours of the scoria cone in the cross-section



observations can be classified into five parts: (1) the central part of the edifice just below the summit crater; (2A–C) the westward, south-southeastward, and north-northeastward extensions from the central part of the edifice; (3) the southwestern edge of the Iwamuroyama lava dome. Figure 9 shows a view of the three-dimensional density image of the Omuroyama scoria cone obtained by multi-directional muography and high density parts. Interpretation of these structures is given in later sections.

Evaluation of the resolution

In order to assess the resolution of the reconstruction results, we simulated the following two cases of simple structures: (a) a scoria cone density of $1.3 \times 10^3 \text{ kg/m}^3$ and density of a 50-m-thick dike is $2.5 \times 10^3 \text{ kg/m}^3$; (b) a scoria cone density of $1.3 \times 10^3 \text{ kg/m}^3$ and density of a cylindrical structure with

a diameter of 100 m is $2.5 \times 10^3 \text{ kg/m}^3$; (c) a scoria cone density of $1.3 \times 10^3 \text{ kg/m}^3$ and density of two cylindrical structures 250 m distant from each other with a diameter of 100 m is $2.5 \times 10^3 \text{ kg/m}^3$. The results are shown in Fig. 10. Two main features were identified. Firstly, the thickness of the dike and radius of the cylinder tend to be blurred over a thickness that is twice the size of these bodies. Secondly, low-density artificial noise occurs around the high-density areas. It was also identified that the two columns, 250 m distant from each other, were clearly distinguished. This should be taken into consideration when interpreting the results of the three-dimensional density reconstructions.

Topographic and geological results

High-resolution topographical map and its interpretation of each topographic feature is shown in Figs. 1b and 11.

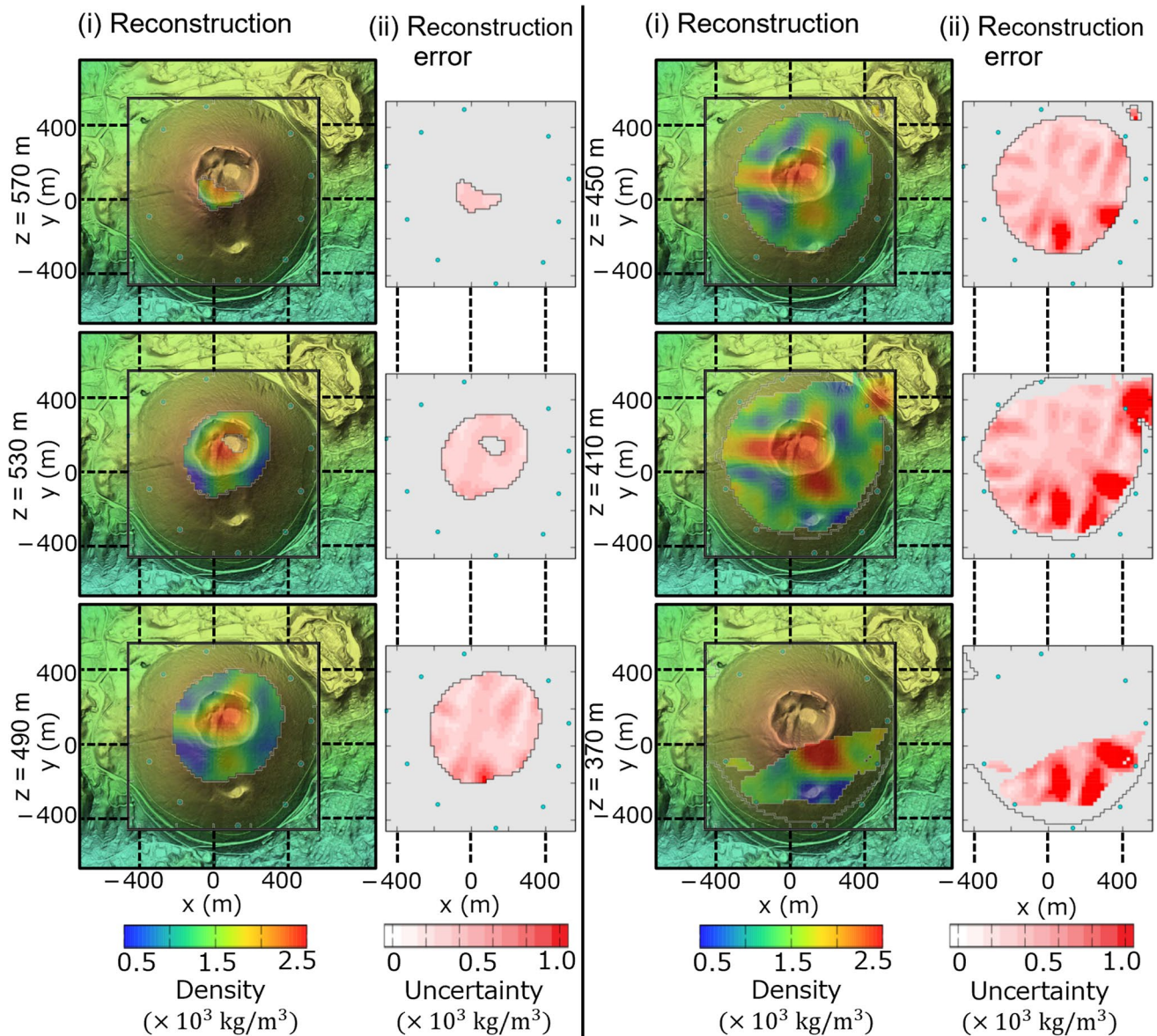


Fig. 8 The three-dimensional density reconstruction results, topography, and estimated overall uncertainties of each elevation section. The blue dots represent the locations of the observation points. (i) Three-

dimensional density reconstruction results shown with 50% transmission in the images. (ii) The overall uncertainties

The ridge at the western foot of the Omuroyama scoria cone (Fig. 1b) was confirmed to be lava flow IV, which emanated from the base of the scoria cone at the end of the eruption (Koyano et al. 1996). We collected samples of this lava flow and measured their density, which was $2.22 \times 10^3 \text{ kg/m}^3$.

The small craters located on the south flank of the scoria cone have a double crater rim (Fig. 1b), indicating that the crater position shifted slightly during the eruption. The shallow trench-like depression extending from the summit crater rim to the south craters is thought to have been caused by slope collapse of surface deposits during the flank eruption.

The topography of the summit crater is rather complex, reflecting the final stage of the eruption (Fig. 11c, d). There is a flat-bottomed depression (i.e., the crater floor). In the outcrop on the northeastern inner wall of this depression, an undeformed spindle-shaped volcanic projectile can be observed in the dense lava flow, which is interpreted to have fallen into the lava lake that previously existed in the crater (Koyano et al. 1996). This means that a lava lake with a level of at least 535 m above sea level existed during the eruption and was then drained at the end of the eruption. Note that the high-density area that may correspond to this lava lake

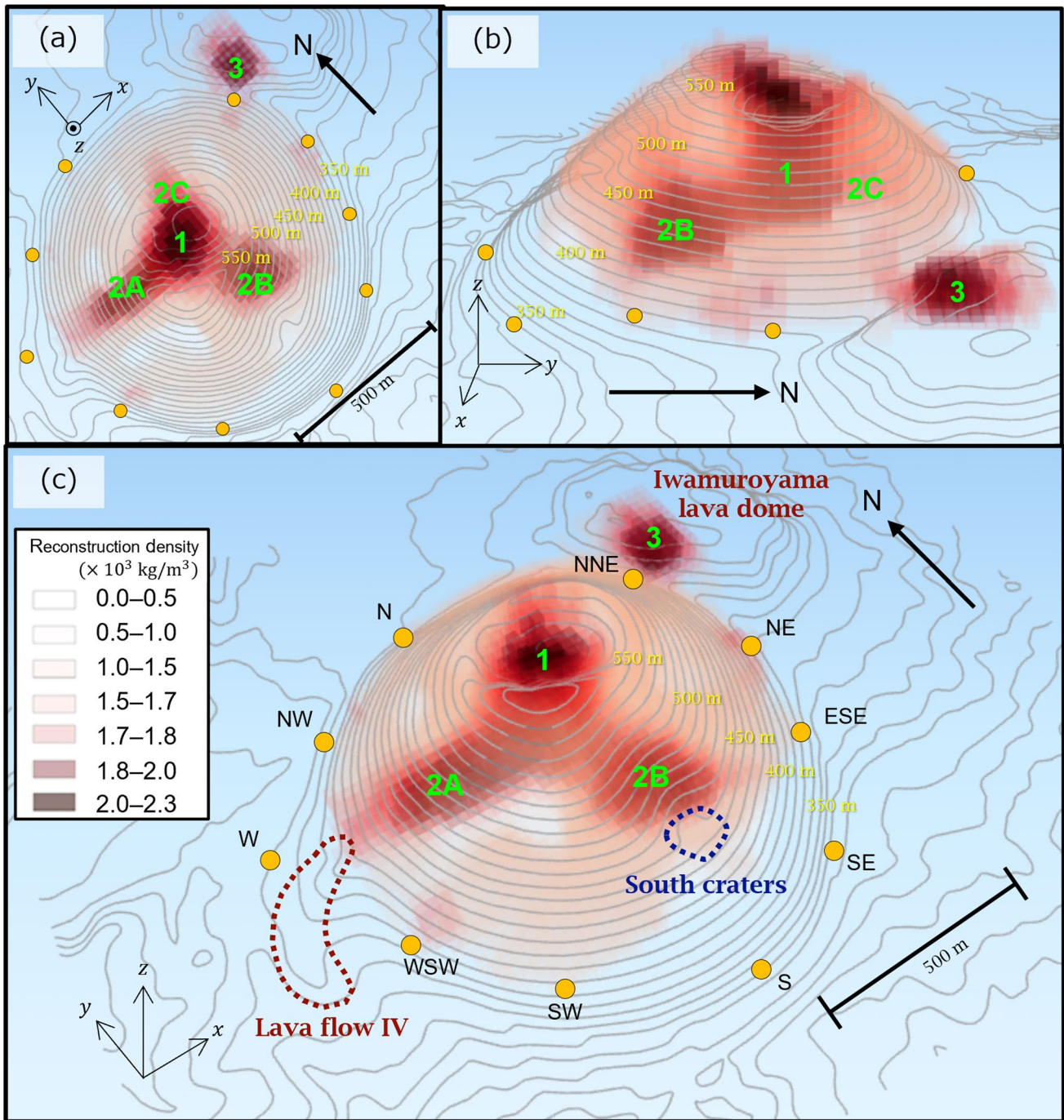


Fig. 9 View of a three-dimensional density image of the Omuroyama scoria cone from **a** the sky above the crater, **b** the eastern sky, and **c** the southwestern sky. The volumes of high density are shown with high opacity. The elevation is scaled to be double that of the horizontal scale. The orange dots represent the locations of the observation points. The green numbers mark the high-density structures. This figure is also viewable at <https://www.eri.u-tokyo.ac.jp/CHEER/data/omuro3ds/>

zonal scale. The orange dots represent the locations of the observation points. The green numbers mark the high-density structures. This figure is also viewable at <https://www.eri.u-tokyo.ac.jp/CHEER/data/omuro3ds/>

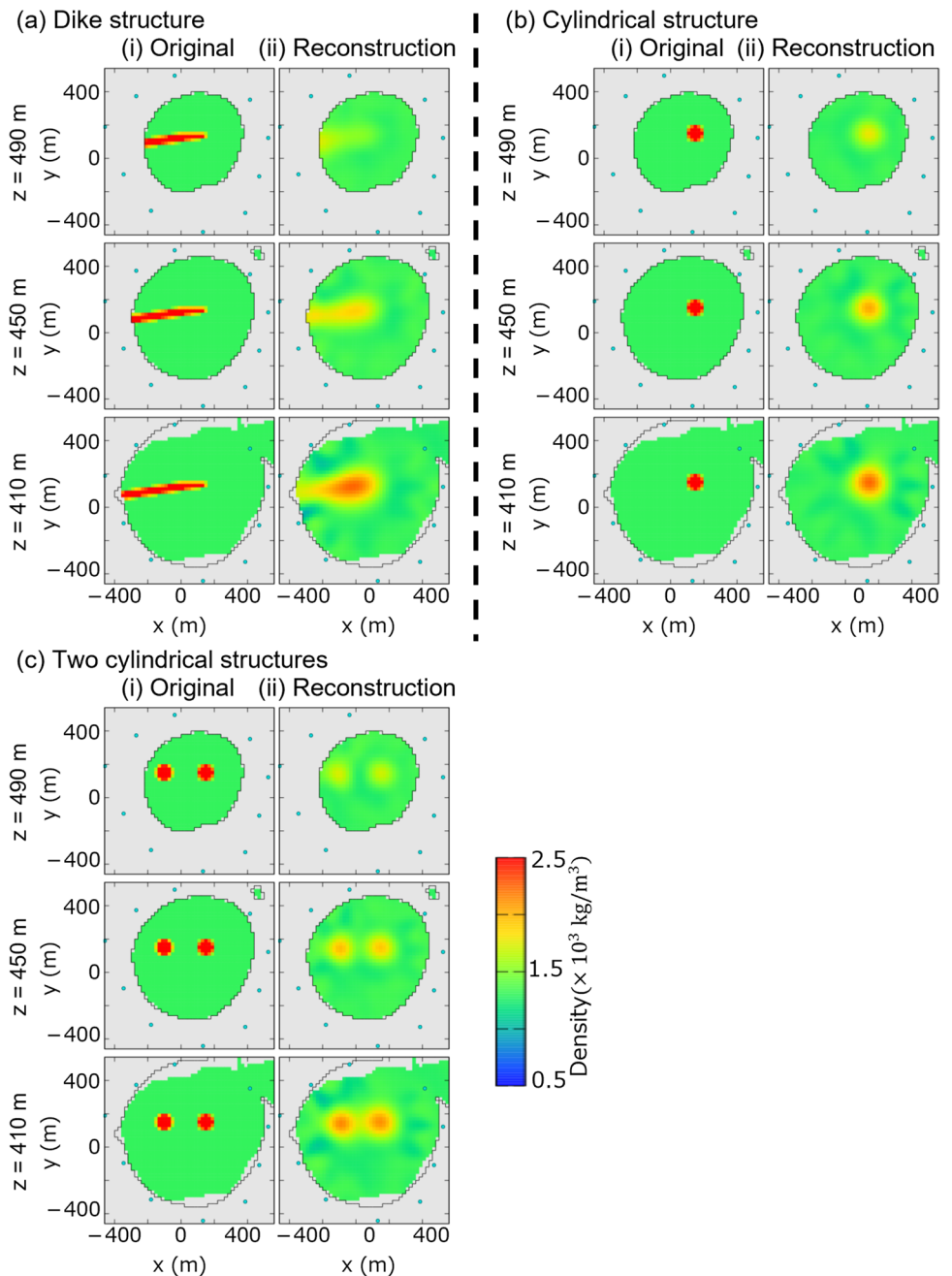
fragment is not visible (Fig. 8), suggesting that this fragment is a minor structure and that the majority of the lava lake has drained back.

which occurs near the northern edge of the crater rim, is thought to be a very small crater produced by a small explosive event. There is also a small cinder cone in the northwestern bottom of the summit crater.

There are several ridges (northern, mid-western, and northeastern) that appear to reflect strongly welded zones near the surface. A small depression (Kitsune-no-oyado),

Northeast of the summit crater, a pit that was 1 m in diameter and 4 m deep was excavated in 2016 (Fig. 12).

Fig. 10 Simulation results for simple structures. The blue dots represent the locations of the observation points. The black line represents the shape of the scoria cone. Indicator (i) is input structure and (ii) is the three-dimensional reconstruction results. **a** The simulation result when the input structure is a dike. **b** The simulation result when the input structure is a cylinder. **c** The simulation result when the input structures are two cylinders



This site is significant because of the lack of large outcrops on the surface of the Omuroyama scoria cone. Most of the outcrop is covered by red and strongly oxidized scoria, with some gray, strongly welded rocks. Samples were collected at depth intervals of 1 m from the pit, which have densities of $1.32\text{--}2.36 \times 10^3 \text{ kg/m}^3$. In general, the density increased with depth. These values are consistent with the value of the three-dimensional density reconstruction.

Discussion

Structure and formation of the Omuroyama scoria cone

In this section, we interpret the results of the three-dimensional density reconstructions (Fig. 9) and discuss the formation of the Omuroyama scoria cone, based on the results of the detailed topographic and geological surveys.

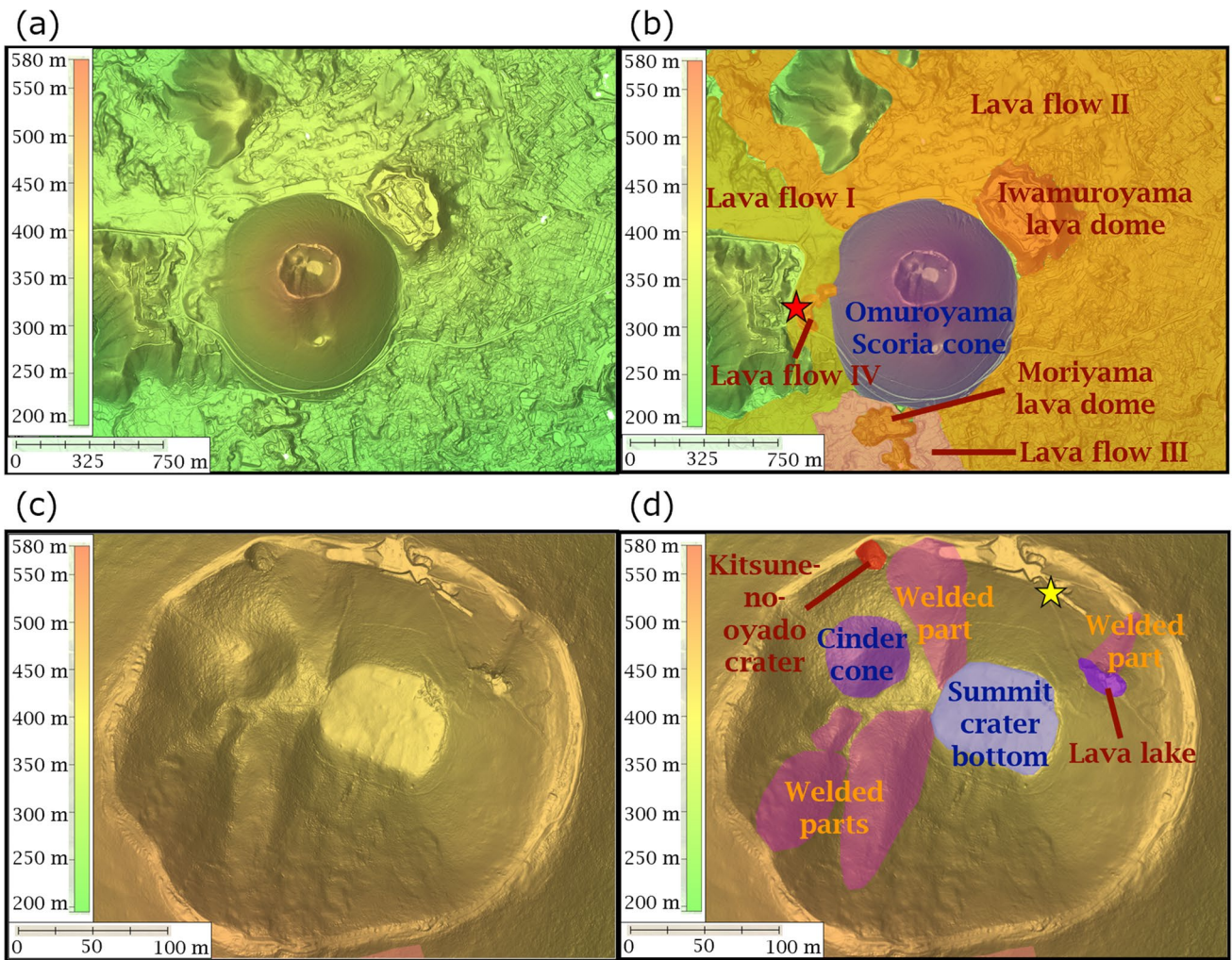
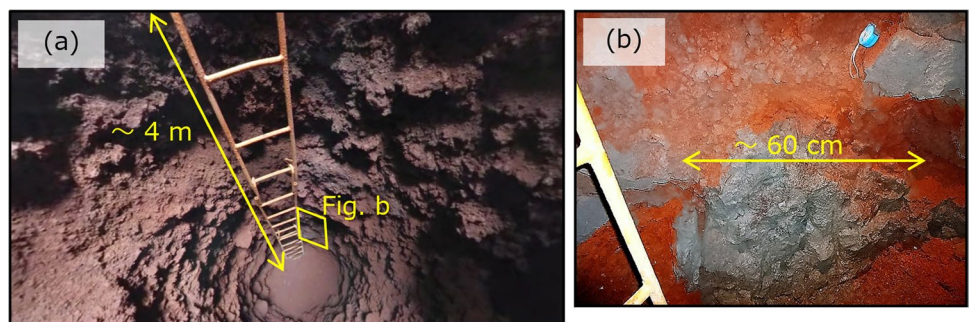


Fig. 11 DEM-based topographic features of the Omuroyama scoria cone and their interpretation. **a** Topographic map around the Omuroyama scoria cone. **b** Topographic features and their interpretations. The red star represents the sampling location of lava flow IV

that was used for density measurements. **c** Topographic map around the summit crater of the Omuroyama scoria cone. **d** Topographic features and their interpretations. The yellow star represents the location of the pit shown in Fig. 10

Fig. 12 Photograph of the summit pit. The location of the pits is shown in Fig. 9. **a** Overview of the 4-m-deep pit. The yellow box shows the area in (b). **b** Close-up view of strongly welded spatter at the bottom of the pit



The central part of the edifice just below the summit crater has a vertical and cylindrical shape and is inferred to be the main vent, which is highly welded. The 2A extension propagates horizontally from the base of the main vent

towards the source of lava flow IV. As such, 2A can be interpreted as being a dike that fed lava flow IV. This implies that draining of the lava lake in the summit crater was caused by the dike intrusion that formed lava flow IV.

The 2B extension also propagates horizontally from the base of the main vent towards the SSW. This feature is also considered to be a dike, but there is no geological evidence for this. However, the small craters on the southern flank might have been supplied by this dike.

The 2C extension is shorter and less clear than the other high-density features. Moreover, it is possible this represents artificial noise, because this is a location where there is no observation point. However, we interpret 2C to represent an incipient dike because of the triaxial elongation of 2A–C, because such a triaxial intrusive structure would be expected to result from expansion of the volcanic edifice caused by magma input during the eruption.

Similar three-directional dike systems have been observed in other volcanoes worldwide, including at Shiprock (Navajo Volcanic Field, northwestern New Mexico: Townsend et al. 2015), Hawaii (Wyss 1980), and the Canary Islands (Carracedo and Troll 2013). The Higashi–Izu monogenetic volcano field, in which the Omuroyama scoria cone occurs, is located in a NW–SE compressional stress field caused by the collision between the Izu and Honshu arcs, and has vent alignments of the same azimuth (Koyama and Umino 1991). This situation appears to be inconsistent with the radial orientation of the dikes associated with the eruption of the Omuroyama scoria cone. While volcanic edifices without significant relief tend to develop subparallel dike swarms consistent with the regional tectonic trend, edifices with subcircular topographic relief are characterized by radial dikes under limited regional stress control (Acocella and Neri 2008). Since the Omuroyama scoria cone is an isolated mountain, its interior and surroundings are less susceptible to the influence of the regional stress field and thus was probably affected by the local stress field caused by magma ascent, producing the radial dikes.

Although the high-density feature (3) is associated with a large error ($> 1.0 \times 10^3 \text{ kg/m}^3$), this structure is consistent with the Iwamuroyama plug dome that formed at the end of the lava eruptions due to the increased lava viscosity.

Based on the above, a tentative history of the formation of the Omuroyama scoria cone is proposed (stages C–E outlined in introduction). Stages A and B that occurred prior to construction of the scoria cone were not considered. Most of the scoria cone was formed during stage C when lava flow I was also effused in the early part of this stage (Fig. 13a). In stage D, lava flows II and III were effused from the northeastern and southern foot of the volcano, respectively (Fig. 13b). Both lava flows are distant from the center of the Omuroyama scoria cone, unlike lava flow I. Therefore, it is reasonable to assume that the lava flows were fed by a two-directional radial dike intrusion from the central vent. This dike intrusion would have been sourced from the deeper part of the Omuroyama central vent, but the latter is not visible in our muographic observations.

Two lava domes (i.e., plug domes), Iwamuroyama and Moriyama, were formed at the outlets of lava flows II and III, respectively, due to the increase in lava viscosity when the lava flows stopped. As a result, dike penetration ceased, and the magma ascended to form a lava lake in the summit crater (Fig. 13c).

In stage E, a further increase in pressure caused radial dikes to intrude from the central conduit in three directions, which were to the NNE, W, and SSE (Fig. 13d). The W-propagating dike formed lava flow IV at the western foot of the cone. The SSE-propagating dike formed a small crater on the southern flank of the cone. The decrease in pressure caused by the formation of these dikes led to the lava lake in the summit crater becoming drained (Fig. 13e).

Even after the lava lake drained, the area around the central conduit remained hot and welding proceeded to form a high-density area in the central part of the edifice. The remaining magma and volcanic gases formed small pyroclastic deposits and craters in the western part of the summit.

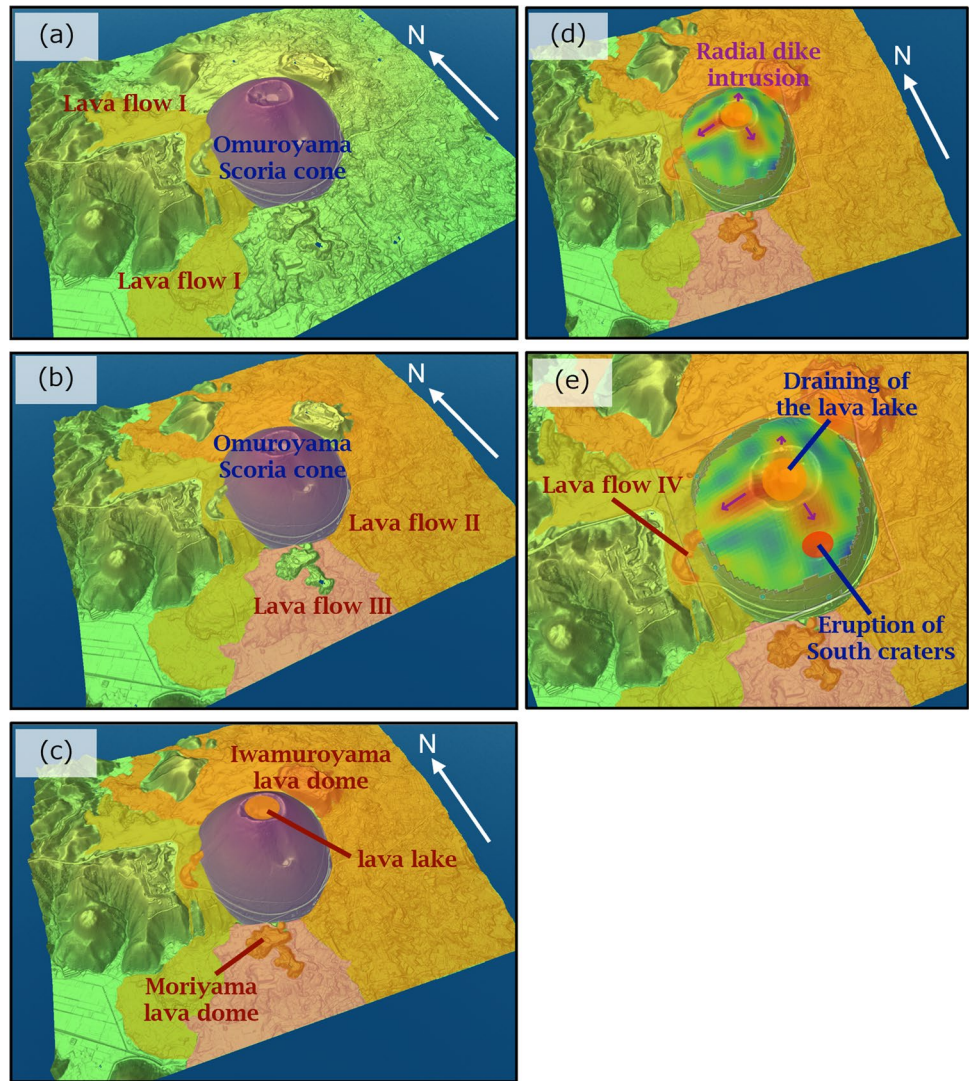
Possibility of applying multi-directional muography to disaster mitigation

Let us consider possible applications of multi-directional muography to volcano disaster mitigation. One main result of this study was the visualization of the relationship between the formation of dikes within the volcanic edifice and eruptive processes of the scoria cone, particularly the lava flows at the foot of the cone and formation of flank craters.

Lava flows from the base of volcanos, not only scoria cone, can be a major risk to residential areas, and such flows can lead to collapse of the volcanic edifice. In a scenario focused on the summit eruption, the sudden occurrence of flank eruptions can also be significant. Therefore, it is important for volcanic disaster mitigation to forecast the phenomena that may occur on the flank and surrounding the volcano during an eruption. However, it has been difficult to detect magma movement occurring inside such volcanos. To what extent can multi-directional muography contribute to solving these problems?

First, we discuss the spatial resolution of muography. The Omuroyama scoria cone is a rare example where muon detectors can be installed around the volcanic edifice from all directions. In most cases, the topography, vegetation, and access limit the observation directions. Therefore, in the case of real volcanoes, it is difficult to select the location of observation points that can provide the required resolution. When the number of observation directions is small, the resolution is low (Nagahara and Miyamoto 2018). Observation direction bias causes density bias as seen in Fig. 7. To overcome such cases, it is required to develop an analytical method to obtain three-dimensional density reconstruction

Fig. 13 The five major stages of development of the Omuroyama scoria cone. **a** Stage C when most of the scoria cone was formed and lava flow I was effused. **b** Stage D when lava flows II and III were effused. **c** Lava effusion ceased and the magma ascended to form a lava lake in the summit crater. **d** Stage E when a further pressure build-up caused radial dikes to intrude outward from the central conduit in three directions. **e** The W-propagating dikes that formed lava flow IV. The SSE-propagating dike caused an eruption and formation of the small craters on the southern flank of the scoria cone. The pressure decrease due to the formation of the dikes caused the lava lake in the summit crater to drain



that reduces the bias even when the location of observation points is not ideal.

Next, it is necessary to mention the temporal resolution that current muographic techniques have reached: Tanaka et al. (2014) succeeded in detecting the ascending and descending of the magma head of Satsuma Iwo Jima volcano in Japan as time-lapse movies taken every 3 days. Also, Jourde et al. (2016) successfully detected fluid movement due to hydrothermal system activity at La Soufriere volcano, Guadeloupe, France, with a temporal resolution of 1 week. Current techniques are still inadequate because the time scale for lava to flow outward from a scoria hill due to dyke intrusion is often shorter than 1 day. Improving the temporal resolution of muography also requires increasing the number of detected muons that penetrate the mountain body.

On the other hand, the flux of cosmic ray muons is limited, the area of the sensitive detection surface must be increased. Also, in order to increase the effective solid angle, the detector must be placed as close to the volcano

as possible. However, it is usually difficult to approach an active volcano. Therefore, it is necessary to develop techniques for remote installation of muon detectors. In addition, multi-directional observations require more muon detectors than in the previous studies described above. Therefore, making 3D density image with higher temporal resolution than these previous studies by multi-directional muography still has a lot of technical challenges to be solved.

Possibility of applying multi-directional muography to other targets

Let us consider about the application of multi-directional muography to other fields. As described in section evaluation of the resolution, in Omuroyama, we were able to detect structures larger more than 100 m for a density difference of about 2 times. Therefore, objects that are similar in size and density difference to the vent of Omuroyama are expected to be detectable. Such examples include volcanoes as well

as archeological sites (Khufu's Pyramid; Morishima et al. 2017) and nuclear reactors (Fukushima Daiichi; Fujii et al. 2022).

To detect smaller structures, it is required to increase the number of observation directions since the detectable structure size strongly depends on it (Nagahara and Miyamoto, 2018). For example, to halve the diameter of the detectable structure, it is required to increase the number of observation directions by four times.

On the other hand, when density differences are small, the uncertainty of the image should be reduced. In this case, not only should the number of observation directions be increased, but the error in the muographic image at each observation point should be reduced. This requires increasing the number of muons observed at each station. The accidental error in muography at each station depends on the statistics of the muon. For example, to halve this error, it is required to increase the muon statistics by four times.

Conclusions

Muographic observations were obtained from 11 directions of the Omuroyama scoria cone, and three-dimensional density reconstructions were made of the data collected from 10 of the 11 directions that were successfully observed. A high-density cylindrical region exists just below the summit crater in the central part of the scoria cone, from which two prominent high-density zones extend to the W and SSE, and a small high-density zone also extends to the NNE. Based on these results and topographical and geological surveys, we constrained the formation of the Omuroyama scoria cone.

One main result of this study was the visualization of the relationship between the formation of dikes within the volcanic edifice and eruptive processes of the scoria cone, particularly the lava flows at the foot of the cone and formation of flank craters. It is important for volcanic disaster mitigation to forecast the phenomena that may occur on the flank and surrounding the volcano during an eruption. Since it has been difficult to directly detect such features in the past, multi-directional muography has resulted in providing one hope.

As mentioned in the previous section, current muography has a time resolution of only a few days, making it difficult to detect signs of a rapid change of eruption in advance even with multi-directional muography. It is also difficult in real active volcanoes to install a large number of detectors surrounding a very close location of the volcano in order to obtain high resolution. However, if more muon fluxes can be detected in a shorter time and detectors can be remotely installed at active volcanoes with improved detectors in the future, it will be possible to confirm the stability of scoria

cones once formed, for example, or to detect signs of collapse in the interior of a mountain with sufficient lead time.

In addition, this study demonstrates that detailed three-dimensional density reconstructions can be obtained from muographic observations in multiple directions. This approach can be widely applied in other fields, such as the investigation of archeological sites and other structures.

Acknowledgements The authors thank Hideaki Aoki and his colleagues of Ike-kankou for giving us permission to observe the Omuroyama scoria cone. We thank Masakazu Ichikawa of the Earthquake Research Institute, the University of Tokyo, for support during the observation campaign. We also thank the staff and students in the F-lab, Nagoya University, for technical assistance with the emulsion films. We also thank the two reviewers and the editor who help us to improve the original manuscript.

Funding Information This research was funded by JSPS KAKENHI Grant 19H01988, an Izu Peninsula Geopark Academic Research Grant (2018), the Joint Research Program of the Institute of Materials and Systems for Sustainability at Nagoya University (2017–2021), and a JSPS Fellowship (Nagahara; Grant DC2; 19J13805).

Open Access This article is licensed under a Creative Commons Attribution 4.0 International License, which permits use, sharing, adaptation, distribution and reproduction in any medium or format, as long as you give appropriate credit to the original author(s) and the source, provide a link to the Creative Commons licence, and indicate if changes were made. The images or other third party material in this article are included in the article's Creative Commons licence, unless indicated otherwise in a credit line to the material. If material is not included in the article's Creative Commons licence and your intended use is not permitted by statutory regulation or exceeds the permitted use, you will need to obtain permission directly from the copyright holder. To view a copy of this licence, visit <http://creativecommons.org/licenses/by/4.0/>.

References

- Acocella V, Neri M (2008) Dike propagation in volcanic edifices: overview and possible developments. *Tectonophysics* 471:67–77 <https://doi.org/10.1016/j.tecto.2008.10.002>
- Ambrosino F, Anastasio A, Bross A, Béné S et al (2015) Joint measurement of the atmospheric muon flux through the Puy de Dôme volcano with plastic scintillators and resistive plate chambers detectors. *J Geophys Res: Solid Earth* 120:7290–7307. <https://doi.org/10.1002/2015JB011969>
- Barde-Cabusson S, Bolós X, Pedrazzi D, Lovera R et al (2013) Electrical resistivity tomography revealing the internal structure of monogenetic volcanoes. *Geophys Res Lett* 40:2544–2549. <https://doi.org/10.1002/grl.50538>
- Bolós X, Delgado-Torres A, Cifuentes G, Macías J L et al. (2020). Internal structure and hydrothermal fluid circulation of Parícutin volcano, Mexico: insights gained from near-surface geophysics. *Geophys Res Lett* 47(16) <https://doi.org/10.1029/2020GL089270>
- Carloganu C, Niess V, Béné S, Busato E et al (2013) Towards a muon radiography of the Puy de Dôme. *Geosci Instrum Method Data Syst* 2:55–60. <https://doi.org/10.5194/gi-2-55-2013>
- Carracedo JC, Troll VR (2013) Structural and geological elements of Teide Volcanic Complex: rift zones and gravitational collapses. Carracedo JC, Troll VR (eds.) *Teide Volcano, Active Volcanoes*

- of the World. (pp. 57–74). Springer, Berlin, Heidelberg. https://doi.org/10.1007/978-3-642-25893-0_4
- Delcamp A, van Wyk de Vries B, Stéphane P, Kervyn M (2014) Endogenous and exogenous growth of the monogenetic Lemptégy volcano, Chaîne des Puys, France. *Geosphere* 10:998–1019 <https://doi.org/10.1130/GES01007.1>
- Fujii H, Hara K, Hayashi K, Kakuno H et al. (2022) Daichi Yamada, Study of the Unit-3 nuclear reactor of Fukushima Daiichi by cosmic muon radiography. *Prog Theor Exp Phys* 2022(1):013C02 <https://doi.org/10.1093/ptep/ptab109>
- Groom DE, Mokhov NV, Striganov SI (2001) Muon stopping power and range tables 10 MeV–100 TeV. *Atom Data Nucl Data Table* 78:183–356. <https://doi.org/10.1006/adnd.2001.0861>
- Hamada K, Fukuda T, Ishiguro K, Kitagawa N. (2012) Comprehensive track reconstruction tool “NETSCAN 2.0” for the analysis of the OPERA Emulsion Cloud Chamber. *J Instrum* 7:P07001 <https://doi.org/10.1088/1748-0221/7/07/P07001>
- Hashimoto T, Utsugi M, Komori S (2009) On the inner structure and formation process of Komezuka scoria cone, Aso volcano. Report of the Joint Geophysical and Geochemical Observations of Aso Volcano (April, 2008–March, 2009), 43–55
- Honda M, Kajita T, Kasahara K, Midorikawa S (2004) New calculation of the atmospheric neutrino flux in a three-dimensional scheme. *Phys Rev D* 70:043008. <https://doi.org/10.1103/PhysRevD.70.043008>
- Kereszturi G, Nemeth K (2013). Monogenetic Basaltic Volcanoes: genetic classification, growth, geomorphology and degradation. In *Updates in Volcanology—New Advances in Understanding Volcanic Systems*, Intech Open Book Series. <https://doi.org/10.5772/51387>
- Kereszturi G, Nemeth K (2016) Sedimentology, eruptive mechanism and facies architecture of basaltic scoria cones from the Auckland Volcanic Field (New Zealand). *J Volcanol Geoth Res* 324(2016):41–56. <https://doi.org/10.1016/j.jvolgeores.2016.05.012>
- Jourde K, Gibert D, Marteau J, De Bremond DJ, Komorowski JC (2016) Muon dynamic radiography of density changes induced by hydrothermal activity at the La Soufrière de Guadeloupe volcano. *Sci Rep* 6:1–12. <https://doi.org/10.1038/srep33406>
- Koyama M, Umino S (1991) Why does the Higashi-Izu monogenetic volcano group exist in the Izu Peninsula?: Relationships between late Quaternary volcanism and tectonics on the northern tip of the Izu-Bonin arc. *J Phys Earth* 39:391–420. <https://doi.org/10.4294/jpe1952.39.391>
- Koyano Y, Hayakawa Y, Machida H (1996) The eruption of Omuroyama in the Higashi Izu monogenetic volcano field. *J Geography (Chigaku Zasshi)* 105:475–484. https://doi.org/10.5026/jgeography.105.4_475
- McGetchin TR, Settle M, Chouet BA (1974) Cinder cone growth modelled after North East Crater, Mt. Etna. *Sicily J Geophys Res: Solid Earth* 79:3257–3272. <https://doi.org/10.1029/JB079i023p03257>
- Miyamoto S, Nagahara S, Morishima K, Nakano T et al (2022) A muographic study of a scoria cone from 11 directions using nuclear emulsion cloud chambers. *Geosci Instrum Method Data Syst* 11:127–147. <https://doi.org/10.5194/gi-11-127-2022>
- Morishima K, Kuno M, Nishio A, Kitagawa N et al (2017) Discovery of a big void in Khufu’s Pyramid by observation of cosmic-ray muons. *Nature* 552:386–390. <https://doi.org/10.1038/nature24647>
- Nagahara S, Miyamoto S (2018) Feasibility of three-dimensional density tomography using dozens of muon radiographies and filtered back projection for volcanoes. *Geosci Instrum Method Data Syst* 7:307–316. <https://doi.org/10.5194/gi-7-307-2018>
- Niess V (2022) The PUMAS library. *Comput Phys Commun* 279(2022):108438. <https://doi.org/10.1016/j.cpc.2022.108438>
- Nishiyama R, Tanaka Y, Okubo S, Oshima H et al (2014a) Integrated processing of muon radiography and gravity anomaly data toward the realization of high-resolution 3-D density structural analysis of volcanoes: case study of Showa-Shinzan Lava Dome, Usu, Japan. *J Geophys Res: Solid Earth* 119:699–710. <https://doi.org/10.1002/2013JB010234>
- Nishiyama R, Miyamoto S, Naganawa N (2014b) Experimental study of source of background noise in muon radiography using emulsion film detectors. *Geosci Instrum Method Data Syst* 3:29–39. <https://doi.org/10.5194/gi-3-29-2014>
- Nishiyama R, Taketa A, Miyamoto S, Kasahara K (2016) Monte Carlo simulation for background study of geophysical inspection with cosmic-ray muons. *Geophys J Int* 206:1039–1050. <https://doi.org/10.1093/gji/ggw191>
- Nishiyama R, Miyamoto S, Okubo S, Oshima H et al. (2017) 3D density modeling with gravity and muon-radiographic observations in Showa–Shinzan lava dome, Usu, Japan. *Pure Appl Geophys* <https://doi.org/10.1007/s00024-016-1430-9>
- Nishiyama R, Miyamoto S, Nagahara S (2020) Estimation of the bulk density of the Omuro Scoria Cone (eastern Izu, Japan) from gravity survey. *Bull Earthq Res Inst Univ Tokyo* 95:1–7 <https://repository.dl.itc.u-tokyo.ac.jp/record/2000093/files/IHO951401.pdf> (last access: 11 March 2022)
- Oláh L, Tanaka HKM, Ohminato T, Varga D (2018) High-definition and low-noise muography of the Sakurajima volcano with gaseous tracking detectors. *Sci Rep* 8:1–13. <https://doi.org/10.1038/s41598-018-21423-9>
- Petronis MS, Delcamp A, van Wyk de Vries B (2013) Magma emplacement into the Lemptégy scoria cone (Chaîne Des Puys, France) explored with structural, anisotropy of magnetic susceptibility, and paleomagnetic data. *Bull Volcanol* 75:753–774 <https://doi.org/10.1007/s00445-013-0753-y>
- Rosas-Carbajal M, Jourde K, Marteau J, Deroussi S et al (2017) Three-dimensional density structure of La Soufrière de Guadeloupe lava dome from simultaneous muon radiographies and gravity data. *Geophys Res Lett* 44:6743–6751. <https://doi.org/10.1002/2017GL074285>
- Saito T, Takahashi S, Wada H (2003) ¹⁴C ages of Omuroyama volcano, Izu Peninsula. *Kazan* 48:215–219 https://doi.org/10.18940/kazan.48.2_215
- Smith IEM, Nemeth K (2017) Source to surface model of monogenetic volcanism: a critical review. *Monogenetic Volcanism*. *Geol Soc Lond Spec Pub* 446:1–28. <https://doi.org/10.1144/SP446.14>
- Tanaka HKM, Nakano T, Takahashi S, Yoshida J (2007a) Development of an emulsion imaging system for cosmic-ray muon radiography to explore the internal structure of a volcano, Mt. Asama. *Nucl Instrum Methods Phys Res Sect A* 575:489–497. <https://doi.org/10.1016/j.nima.2007.02.104>
- Tanaka HKM, Nakano T, Takahashi S, Takeo M et al. (2007b) High resolution imaging in the inhomogeneous crust with cosmic-ray muon radiography: the density structure below the volcanic crater floor of Mt. Asama, Japan. *Earth Planet Sci Lett* 263(1–2):104–113 <https://doi.org/10.1016/j.epsl.2007b.09.001>
- Tanaka HKM, Nakano T, Takahashi S, Yoshida J et al (2007c) Imaging the conduit size of the dome with cosmic-ray muons: the structure beneath Showa-Shinzan lava dome, Japan. *Geophys Res Lett* 34:L22311. <https://doi.org/10.1029/2007GL031389>
- Tanaka HKM, Uchida T, Tanaka M, Shinohara H et al (2009) Cosmic-ray muon imaging of magma in a conduit: degassing process of Satsuma-Iwojima Volcano, Japan. *Geophys Res Lett* 36:L01304. <https://doi.org/10.1029/2008GL036451>
- Tanaka HKM, Taira H, Uchida T, Tanaka M et al (2010) Three-dimensional computational axial tomography scan of a volcano with cosmic ray muon radiography. *J Geophys Res* 115:B12332. <https://doi.org/10.1029/2010JB007677>

- Tanaka HKM, Kusagaya T, Shinohara H (2014) Radiographic visualization of magma dynamics in an erupting volcano. *Nature Comm* 5:3381 <https://doi.org/10.1038/ncomms4381>
- Tarantola A, Necessian A (1984) Three-dimensional inversion without blocks. *Geophys J Int* 76:299–306. <https://doi.org/10.1111/j.1365-246X.1984.tb05047.x>
- Tioukov V, Alexandrov A, Bozza C, Consiglio L et al (2019) First muography of Stromboli volcano. *Sci Rep* 9:1–11. <https://doi.org/10.1038/s41598-019-43131-8>
- Townsend M, Pollard DD, Johnson K, Culha C (2015) Jointing around magmatic dikes as a precursor to the development of volcanic plugs. *Bull Volcanol* 77:92–104. <https://doi.org/10.1007/s00445-015-0978-z>
- Wyss M (1980) Hawaiian rifts and recent Icelandic volcanism: expressions of plume generated radial stress fields. *J Geophys* 47:19–22
- Yamamoto H (2003) The mode of lava outflow from cinder cones in the Ojika-Jima monogenetic volcano group. *Kazan* 48:11–25
- Yoshimoto M, Nakano T, Komatani R, Kawahara H (2017). Hyper-track selector nuclear emulsion readout system aimed at scanning an area of one thousand square meters. *Prog Theor Exp Phys* 10:103H01 <https://doi.org/10.1093/ptep/ptx131>